Final report

1 General information

DFG reference number: GR 1024/41-1,2, DU 405/17-1,2
Project number: 448085183
Project title: **Numerical modelling of partially cemented soils in the stagnation zone**
Name(s) of the applicant(s):

Jürgen Grabe, Univ.-Prof. Dr.-Ing. (B5)

Alexander Düster, Prof. Dr.-Ing. habil. (M10)

Official address(es):

Hamburg University of Technology (**TUHH**)
Institute of Geotechnical Engineering and Construction Management (**GBT**) (B5)

Schellerdamm 22
21079 Hamburg, Germany

Hamburg University of Technology (**TUHH**)
Numerical Structural Analysis with Application in Ship Technology - Institute for Ship Structural Design and Analysis (**SKF**) (M10)
Am Schwarzenberg-Campus 4(C)
21073 Hamburg, Germany

Name(s) of the co-applicants:
Name(s) of the cooperation partners: Laura De Lorenzis, Prof. Dr., Institute for Mechanical Systems, Department of Mechanical and Process Engineering, ETH Zürich, Switzerland
Reporting period (entire funding period):
01.10.2020 – 30.09.2023, 01.01.2024 – 31.12.2025 (incl. cost-neutral extension of 4 months)

2 Summary

The goal of this project was to experimentally and numerically investigate partially cemented sands in the stagnation zone to better understand their micromechanical behavior. In particular, the project aimed to develop automated numerical frameworks based on the Finite Element Method (FEM) and the Finite Cell Method (FCM), respectively. These tools were ultimately applied to cemented sand samples under uniaxial compressive loading. The project was divided into two phases. In the first phase, only the linear elastic region of the deformations was considered. The goals included material characterization, experimental investigations, acquiring CT scans and analyzing them using image processing, converting the CT images into FE models, developing numerical frameworks using FEM and FCM, respectively, verifying these numerical models, and validating them with experiments. Furthermore, numerical homogenization was employed. In the second phase, the aim was to extend the proposed numerical frameworks to capture failure mechanisms in cemented sands, such as matrix cracking and grain crushing. These complex fracture phenomena required more advanced and robust solution schemes. A larger deformation region was considered, introducing nonlinearities in the material behavior. In addition, full-field, experimentally derived kinematic fields were acquired to enrich the validation dataset. The objectives included enhancing the FEM framework for fracture mechanics through XFEM as well as phase-field modeling, extending the FCM using phase-field modeling, enriching the experimental database by capturing additional image sequences, acquiring full-field experimental data using Digital Volume Correlation (DVC), and validating the numerical results against DVC.

German Version

Das Ziel dieses Projekts war die experimentelle und numerische Untersuchung teilzementierter Sande im Stagnationsbereich, um ihr mikromechanisches Verhalten besser zu verstehen. Insbesondere zielte das Projekt darauf ab, automatisierte numerische Berechnungsmethoden auf Basis der Finite Elemente Methode (FEM) sowie der Finite Cell Methode (FCM) zu entwickeln. Diese Methoden wurden anschließend auf zementierte Sandproben unter uniaxialer Druckbelastung angewendet. Das Projekt wurde in zwei Phasen unterteilt. In der ersten Phase wurde ausschließlich der linear-elastische Bereich der Verformungen betrachtet. Die Ziele umfassten die Materialcharakterisierung, experimentelle Untersuchungen, die Erstellung von CT-Scans sowie deren Auswertung mittels Bildverarbeitung, die Umwandlung der CT-Daten in FE-Modelle, die Entwicklung numerischer Methoden auf Basis von FEM bzw. FCM, die Verifikation dieser

numerischen Modelle sowie ihre Validierung durch Experimente. Zusätzlich wurde eine numerische Homogenisierung durchgeführt. In der zweiten Phase bestand das Ziel darin, die numerischen Berechnungsmethoden zu erweitern, um Versagensmechanismen in zementierten Sanden, wie Matrixrisse und Kornbruch, abzubilden. Diese komplexen Bruchphänomene erforderten fortgeschrittenere und robustere Lösungsmethoden. Ein größeres Deformationsgebiet wurde berücksichtigt, wodurch Nichtlinearitäten im Materialverhalten auftraten. Darüber hinaus wurden experimentell abgeleitete kinematische Felder erfasst, um den Validierungsdatensatz zu erweitern. Die Ziele umfassten die Erweiterung der FEM für Bruchmechanik mittels XFEM sowie der Phasenfeldmethode, die Erweiterung der FCM durch Phasenfeldmethode, die Anreicherung der experimentellen Datenbank durch zusätzliche Bildsequenzen, die Erfassung experimenteller Daten mittels Digital Volume Correlation (DVC) und die Validierung der numerischen Ergebnisse anhand der DVC-Daten.

3 Progress Report

This project aimed to experimentally and numerically investigate partially cemented sands in the stagnation zone. The **first project phase** addressed the linear elastic regime, while the **second project phase** focused on fracture behavior. The following goals were defined:

1. Enhance understanding of micromechanical deformation and fracture in multiphase porous composite sand materials in stagnation zones.
2. Apply and validate numerical modeling techniques based on CT scans.
3. Further develop numerical methods (FCM and FEM) and analysis procedures.
4. Connect microscopic and macroscopic behaviors to improve practical FE models, including the soil-structure transition.
5. Identify anisotropic material properties and stress inhomogeneities of the individual phases of a composite material using numerical methods.

These results are discussed with the other project findings regarding the defined goals.

Experimental investigations (B5)

Consolidated drained triaxial compression tests were carried out as macroscopic laboratory experiments on cemented Hamburg sand to characterise the mechanical behaviour of the stagnation zone of cemented soil volumes. All investigated specimens are in a dense state, with a relative density I_R of 70 %, i.e. the soil structure corresponds to a densely packed sand. The results show that even small amounts of binder fundamentally transform the typical contractant–dilatant response of granular soils into a stiff and clearly brittle behaviour with pronounced peak strength, post-peak softening, macro-cracking and an approximately constant residual shear stress. The binder suppresses irreversible grain rearrangement and contributes directly to load transfer, thereby modifying the failure mechanism compared with uncemented sand. In the second project phase, the dataset for cemented Hamburg sand was completed by additional cementation degrees and a new extensive test series on dense cemented Cuxhaven sand was performed. For both sands, the cementation degree was defined with respect to the pore volume, where 100 % corresponds to the theoretical filling of the total pore volume with cement; conversion to a mass-based measure for better comparability with the literature yields equivalent cementation degrees of about 0–17 %. The experimental datasets are available open access in [B8]. Detailed results, observed trends and a comprehensive comparison between both cemented sands will be reported in [U2]. As an illustration, Fig. 1 evaluates both the elastic stiffness and the deviatoric stresses as a function of the cementation degree for different levels of cementation. The results reveal a clear trend of increasing tangent modulus and deviatoric stress with increasing cementation degree; in absolute terms, both stiffness and strength are consistently higher for cemented Hamburg sand than for the finer Cuxhaven sand (goals 1,4).

Acquisition of CT scans and image-processing (B5)

Within the first project phase, the internal structure of the cemented sand was quantified for different cementation degrees by X-ray CT imaging. Three cylindrical micro-samples ($h = 20\,\mathrm{mm}$, $d = 10\,\mathrm{mm}$) were scanned at Laboratoire 3SR in Grenoble with a spatial resolution of $13\,\mu\mathrm{m}/$ voxel prior to uniaxial compression testing, providing 3D reconstructions of grains, pores, and cement matrix for specimens with cementation degrees $S_{\mathrm{cem}} = 50\,\%$, $70\,\%$, and $100\,\%$ for the dense and loose state. In the second project phase, this CT dataset

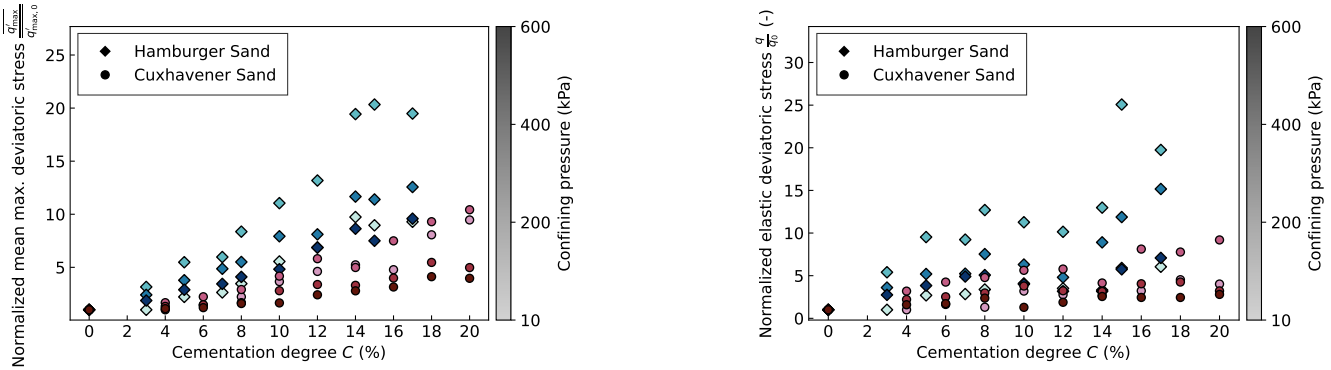

Figure 1: Normalised average maximum deviatoric stress (kPa) (left). Normalized initial stiffness E as a function of mass-based cementation degree C and confining pressure for Hamburg and Cuxhaven sand (left); averages computed from all tests at each confining stress level.

was extended in the same laboratory by specimens with $S_{\text{cem}} = 20\,\%$, $30\,\%$, $40\,\%$, and $80\,\%$ for the dense state, yielding a consistent series that covers a wide range of lower and higher cementation levels (goals 1,2,4).

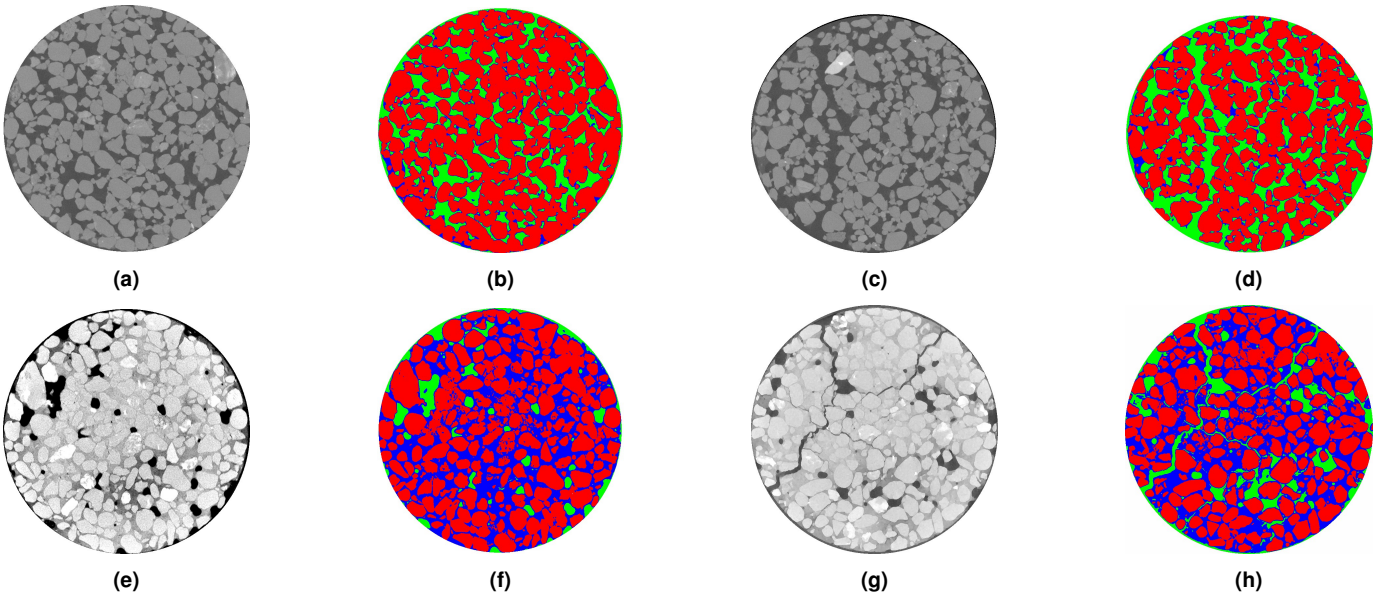

Figure 2: Cross-sections at a given height in the initial state: (a) $S_{\text{cem}} = 20\,\%$ (unsegm.), (b) $S_{\text{cem}} = 20\,\%$ (segm.), (e) $S_{\text{cem}} = 100\,\%$ (unseg.), (f) $S_{\text{cem}} = 100\,\%$ (seg.); and in the final state: (c) $S_{\text{cem}} = 20\,\%$ (unseg.), (d) $S_{\text{cem}} = 20\,\%$ (segm.), (g) $S_{\text{cem}} = 100\,\%$ (unseg.), (h) $S_{\text{cem}} = 100\,\%$ (segm.).

Conversion of CT scans into FE models (B5, M10)

Within the first project phase, an image-adapted finite element (FE) mesh generator was developed to convert segmented CT images of the cemented sand into numerical models. Following the image-adapted meshing technique (IAMT), the Python code uses the CGAL library to create an unstructured FE mesh composed of solid tetrahedral elements (tet4) and interface triangular elements (tri3). Starting from the segmented image, phase boundaries are detected via the gradient of the grey-value field, and two node sets (bulk and interface) are created and triangulated using Delaunay algorithms. Each element is then assigned to a material phase by correlating its barycentre with the underlying voxel label, and mesh-optimization routines are applied to improve element quality. Thus, only one material is assigned per element [A5], [B6] (goals 2,3). The mesh generation in immersed methods like the FCM is straightforward. A simple Cartesian grid is placed directly onto the filtered and segmented CT scans, eliminating the need for complex, geometry-conforming meshing. The in-house simulation software `AdhoC++` is then used to describe the geometry, generate the mesh and perform FCM simulations. To create the input files for `AdhoC++`, the CT scans – originally provided as TIFF-files – are read and converted into an ASCII-based voxel file using the open-source Python package SPAM [L1].

Development of numerical frameworks based on FEM & FCM for linear elastic simulations (B5, M10)
The image-adapted meshes were converted into a generic FE input format and used to perform mesoscale simulations with the FE code ABAQUS. Air pores and interface elements were omitted so that the remaining phases are perfectly bonded. Quartz grains and diluted cement matrix were modelled as linearly elastic materials, with stiffness values in the GPa range for the grains and in the order of some tens of MPa for the cement, calibrated against the uniaxial compression tests. Mesh-dependency was assessed by varying the nodal density in uniaxial compression simulations. The equivalent "spring" stiffness and the global volumetric strain converge to constant values with increasing refinement, demonstrating numerical objectivity. Beyond this verification, the image-based FEM is able to reproduce typical micromechanical phenomena in cemented sands, such as intergranular load transfer, stress transmission and concentration within grains and cement matrix (stress bridges), and the splitting kinematics of shear banding [A4], [B7] (goals 1–3).
The FCM framework was further developed to handle complex and heterogeneous microstructures obtained from CT scans in a fully automated fashion. To this end, several extensions were developed and incorporated into the FCM approach, which are summarized in the following (goal 3). First, to obtain a smooth geometry representation of the CT scans, the L^2-projection was implemented and tested. Here, the global L^2-projection was preferred over the local approach, as it yields a C^0-continuous solution. This C^0-continuity is also required for the enrichment in later stages. The geometry smoothing based on the L^2-projection led to improvements of the results, such as reduced stress oscillations [A1, B2]. Also, the additional numerical effort is small compared to that of the mechanical problem. To account for the different phases (cement matrix, grain particles, and air) of the cemented sands, the extended L^2-projection was developed [A1, B2]. This approach yields two separate level-set functions: ϕ_A, which captures the physical domain, and ϕ_B, which captures the material interfaces. For each level-set function, a standard L^2-projection is then applied. The local enrichment was applied to the FCM to capture the weak discontinuities at the material interface and recover the optimal convergence rate. Specially, the *hp-d*/PUM-FCM based on the cell-wise strategy was adopted [A1]. Here, only cells that are cut by the material interfaces are enriched. Proper treatment of the discontinuities within the numerical integration requires addressing two aspects. First, the enriched cells require a higher integration order, since the enrichment function increases the overall polynomial order. Second, the adaptive spacetrees (quadtree/octree in 2D/3D) must also take into account the material interfaces, in addition to the indicator function of the FCM. For heterogeneous voxel-based microstructures, the enrichment function is constructed from the level-set function ϕ_B, obtained via the extended L^2-projection. The enrichment was tested on a 3D benchmark consisting of a box with spherical inclusion, using an exact geometry representation, and it was verified against an analytical solution [A1]. The results showed that enrichment improved the FCM, yielding more accurate stress predictions.

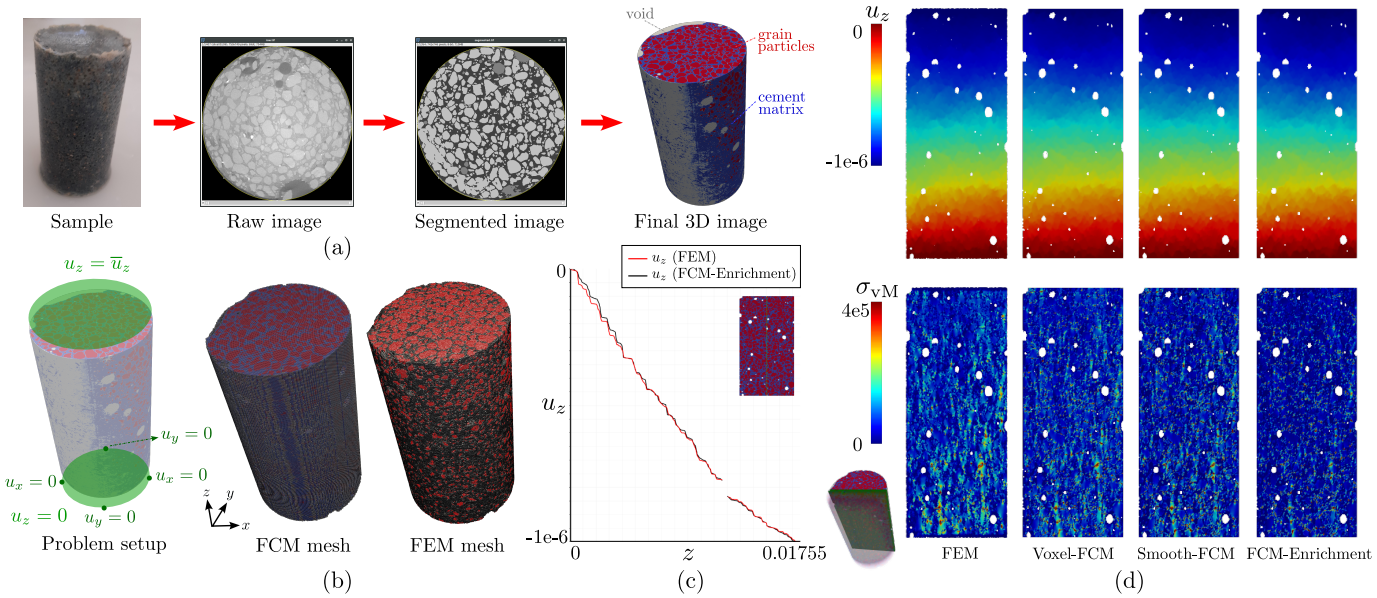

Figure 3: Automated FEM/FCM simulation pipeline illustrated for sample $S_{cem} = 100\,\%$. (a) image processing, (b) setup and meshes, (c) verification, and (d) displacement and stress contours.

The proposed approaches were applied to several examples of cemented sands under uniaxial compressive loading, including 2D axisymmetric simulations of the sample $S_{\text{cem}} = 100\,\%$ [A4], as well as 3D simulations based on a simplified glass beads geometry [A1, B2]. The material properties, boundary conditions, and loading were defined according to the experimental setup. Three versions of the FCM were considered: (1) a voxel-based FCM applied directly to the CT scan (*Voxel-FCM*), (2) an FCM with geometry smoothing via extended L^2-projection (*Smooth-FCM*), and (3) an FCM with geometry smoothing combined with local enrichment (*FCM-Enrichment*). The same mesh was used for the FCM, the enrichment, and the L^2-projection. In addition, the interpolation order of the enrichment function was chosen to match the order of the L^2-projection. The investigations showed that the L^2-projection and local enrichment reduced stress oscillations and thereby improved the FCM results. Furthermore, the FCM versions were compared to the mesoscale FEM approach [A4], yielding a good agreement between the two methods (goal 2). Finally, the developed frameworks were utilized to investigate the micromechanical effects in cemented sands under uniaxial compression [A1, A4, B2]. The investigations revealed that the stresses are primarily transmitted through contact between neighboring grain particles, forming narrow stress bridges within the intermediate cement matrix. These phenomena can trigger failure mechanisms such as matrix cracking and grain crushing (goals 1,5). An automated FEM/FCM simulation pipeline of the whole procedure is shown in Fig. 3. Furthermore, large-scale 3D simulations of the sample $S_{\text{cem}} = 100\,\%$ were performed using the developed FCM framework. As an efficient iterative solver, the preconditioned conjugate gradient method (PCG) with an Additive-Schwarz preconditioner was employed [L2]. Moreover, massive parallelization based on a hybrid MPI/OpenMP approach was adopted to generate the mesh, solve the system and perform post-processing. The computations were carried out on supercomputers of NHR@ZIB (goals 1 – 3). The results are being prepared for a manuscript to be submitted to a journal.

Moreover, several integration schemes were further developed and investigated (goal 3). The adaptive spacetrees used for the numerical integration of the enriched FCM produce a large number of integration points and thus, can become very expensive. To address this issue, moment fitting (MF) schemes were employed, which compute individual quadrature rules for each cut finite cell, resulting in a small set of integration points. However, MF schemes had previously been developed only for single-material domains. In this project, MF schemes were extended to heterogeneous materials via domain decomposition. The idea is to apply MF separately to each material phase, leading to the *domain decomposed moment fitting (MFDD)* and *domain decomposed non-negative moment fitting (NNMFDD)*. The proposed methods were tested on a 2D benchmark consisting of a plate with a circular inclusion and were verified against an analytical solution [L3]. The results in Fig. 4 show that both methods provide accurate results while significantly reducing the number of integration points. Moreover, NNMFDD exhibits additional robustness due to its positive quadrature weights.

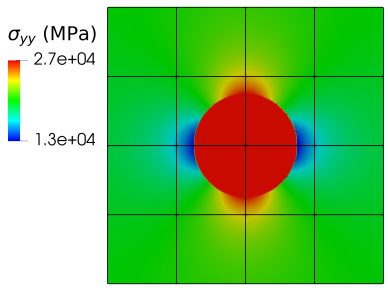

(a)

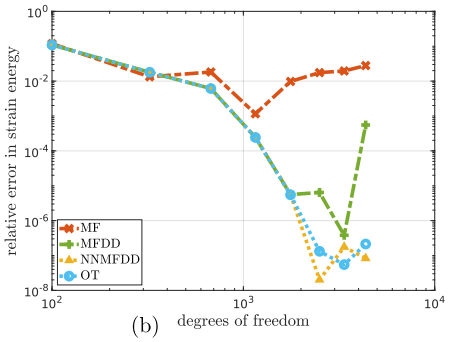

(b)

Scheme	Integration points	Ratio
OT	1,124,332	1
MF	8,820	127
MFDD	8,279	136
NNMFDD	7,945	142

(c)

Figure 4: Plate with circular inclusion. (a) Cauchy stress component σ_{yy} using NNMFDD with FCM mesh, (b) relative error in strain energy $e_r = \left|\frac{\mathcal{U}-\mathcal{U}^{\text{ref}}}{\mathcal{U}^{\text{ref}}}\right|$, and (c) number of integration points.

An alternative integration scheme based on curve mapping using Bézier fitting was also developed and investigated [A2, B4]. This approach showed promising results for numerical examples in 2D and 3D when compared with FEM simulations, demonstrating high potential in cemented sand applications (goal 3).

Numerical homogenization (B5, M10)

To obtain the effective material properties of heterogeneous materials such as cemented sands, numerical

homogenization is utilized both with FCM and FEM. Within the FCM framework, the window method with kinematic uniform boundary conditions (KUBC) was employed. The basic idea is to embed the microstructure inside a window and iteratively update the window's material properties until convergence is achieved. The window has a predefined width and an initial elasticity matrix $\mathbf{C}_{\text{ini}}$. During each iteration, an FCM simulation is performed for every load case. The converged window properties then yield the effective material properties. In this approach, an isotropic behavior was assumed, i.e., the effective Young's modulus E_{eff} and the effective Poisson's ratio ν_{eff} were extracted from the effective elasticity matrix $\mathbf{C}_{\text{eff}}$. However, this approach can be easily adopted to anisotropic materials as well (goals 2, 5).
To accelerate the computations, several strategies were used. First, an improved initial guess was obtained using the rule of mixtures. Next, to reduce the number of iterations, Aitken's Δ^2-method was applied for convergence acceleration. The performance of these approaches was investigated on a 2D benchmark consisting of a plate with a circular hole (Fig. 5a). As expected, these approaches reduce the number of iterations. Since the stiffness matrix must be computed multiple times for each iteration and load case, numerical integration can become very costly, especially for 3D simulations. Therefore, preintegration of the cell stiffness matrices was adopted, drastically reducing the computation time.
Finally, homogenization via FCM was applied to a *Testing Volume Element (TVE)* of the cemented sand sample $S_{\text{cem}} = 100\,\%$, to compute its effective material properties (Fig. 5b). The TVE microstructure consists of 154 voxels in each direction, with a voxel size of $13\,\mu m$, resulting in a side length of $L = 2\,\text{mm}$. The window size t_w was chosen as 20% of the side length. The FCM results were compared to those obtained from the mesoscale FEM and the experiments (goal 2), as shown in Fig. 5c. From the experimental data, the effective Young's modulus was determined as $E_{\text{eff}} = 1072\,\text{MPa}$. Using FCM with $p = 2$ and NVC $= 14$ voxels per cell in each direction yields $E_{\text{eff}} = 1107\,\text{MPa}$, which is very close to the experimental reference (with relative error of $\sim 3\,\%$). Furthermore, the FCM benefits from the acceleration methods, reducing the number of required iterations as well as computation time.

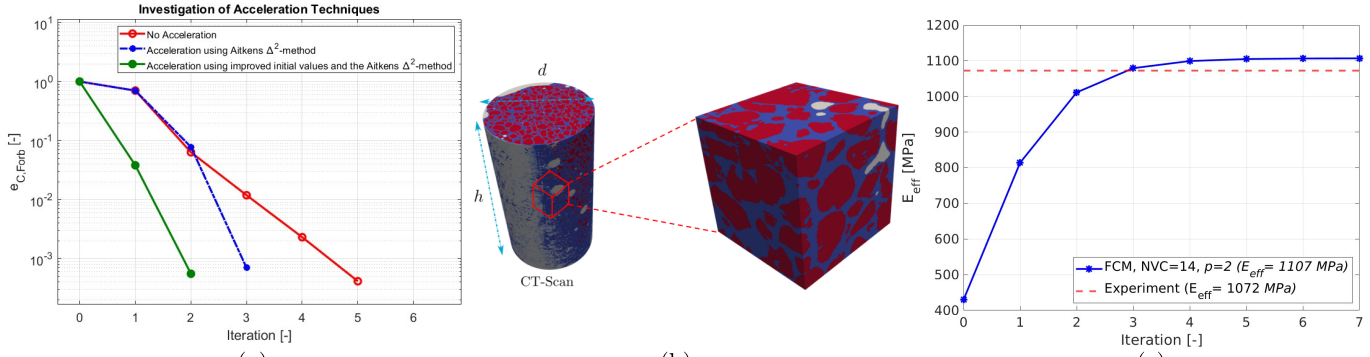

Figure 5: Homogenization based on FCM and window method. (a) Investigation on 2D benchmark (plate with a hole). Relative error: $e_{C,Forb} = \frac{\|\mathbf{C}_{\text{eff}} - \mathbf{C}_{\text{ini}}\|_F}{\|\mathbf{C}_{\text{ini}}\|_F}$ with Frobenius norm $\|\mathbf{C}\|_F = \sqrt{\sum_{i,j=1}^{n} |C_{ij}|^2}$. Application on 3D cubic TVE of cemented sand sample $S_{\text{cem}} = 100\,\%$. (b) TVE extraction of CT scan, and (c) validation with experiments.

The complementary study was carried out on the same CT–based microstructure of the fully cemented sand specimen ($S_{\text{cem}} = 100\,\%$) using a standard finite element formulation. Choosing the same TVE as for FCM, the individual phases air, sand grains and cement paste were converted into a conforming tetrahedral FE mesh. Analogously to the FCM window approach, this heterogeneous TVE was embedded in a homogeneous surrounding window whose material properties were treated as unknown and updated iteratively. The FE simulations employed the same kinematic uniform boundary conditions as the FCM model. From the reaction forces at the inner window boundary, the effective stiffness matrix of the window, $\mathbf{C}_{\text{eff}}$, was evaluated. Assuming isotropic behaviour—again in direct analogy to the FCM part—the effective Young's modulus E_{eff} and Poisson's ratio ν_{eff} were extracted from the components C_{11} and C_{12} of $\mathbf{C}_{\text{eff}}$ by standard isotropic relations. The corresponding iterative workflow, including the update of E and ν and the stopping criterion based on the relative change in E, is summarized in the flowchart in Fig. 6. A parametric study was performed with different window thicknesses between $10\,\%$ and $50\,\%$ of the TVE edge length, and with several mesh refinement levels (parameter *SD*). For each configuration, the algorithm was started from an initial guess for E and ν and iterated until the relative change in Young's modulus fell below a prescribed tol-

erance. The convergence histories of E_{eff} and ν_{eff} for all combinations of window thickness and refinement are depicted in Fig. 7. The plots demonstrate that the iterative scheme is numerically robust: for all cases, both E_{eff} and ν_{eff} approach stable plateau values within only a few iterations, and finer meshes mainly lead to a slight increase in the converged stiffness but do not change the qualitative behaviour. The influence of the window thickness is particularly evident in the upper row of Fig. 7, where E_{eff} is plotted versus iteration. Very thin windows (10 % of L) yield noticeably underestimated effective Young's moduli, indicating that boundary effects are still dominant. With increasing window thickness the curves shift upwards, and a window thickness of about 20 % of the TVE edge length emerges as a good compromise: for sufficiently refined meshes the converged E_{eff} is in very good agreement with the experimental reference value of approximately 1072 MPa obtained from CT–based uniaxial compression tests on the same specimen. Thicker windows ($30 - 50$ %) lead again to slightly smaller moduli, whereas the effective Poisson's ratio remains almost constant at about $\nu_{\text{eff}} \approx 0.10$ for all configurations (lower row of Fig. 7). Overall, the FE–based window homogenization confirms the FCM results discussed above and the experimentally measured stiffness of the fully cemented sand. The FE study and the convergence plots in Fig. 7 underline that the window method provides a consistent and reliable framework for upscaling the CT–resolved microstructure of cemented sands. The implementation based on the workflow in Fig. 6 also establishes a flexible tool chain that can be extended in future work to partially cemented microstructures and to non–linear constitutive laws (goals 2, 4).

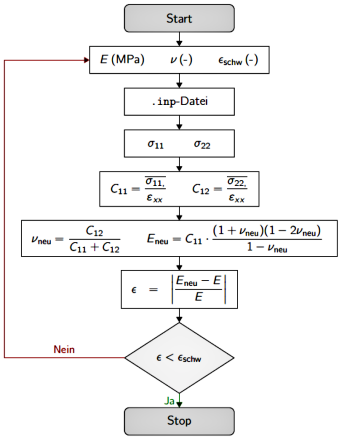

Figure 6: Workflow of the FEM-based homogenization procedure.

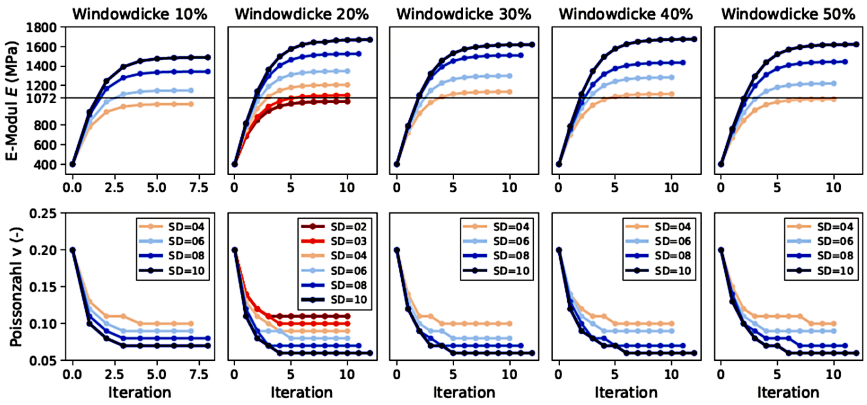

Figure 7: Simulation results of Young's modulus and Poisson's ratio for different window thicknesses and mesh refinements (SD = 2: mesh size of $2 \times 13\,\mu$m; SD = 10: mesh size of $10 \times 13\,\mu$m).

Acquisition of full-field experimental kinematic fields using DVC (B5)

In the second project phase, Digital Volume Correlation (DVC) was applied to all available CT datasets. The analysis was carried out with the open-source Python package SPAM [L1], developed at Laboratoire 3SR in Grenoble, which provides 3D tomographic image-correlation tools. The main objective was to obtain full-field displacement maps of the cemented sand samples, from which strain measures were derived in post-processing by evaluating the DVC results in ParaView. A direct correlation of the initial, unloaded configuration with the final state at failure proved problematic, especially for highly cemented, brittle specimens. Crack formation causes strong changes of the voxel pattern and displacement discontinuities, whereas the global DVC formulation in SPAM assumes a continuous displacement field described by linearised deformation mappings within each correlation element. As a result, the iterative correlation often did not converge or produced unreliable results, particularly for strongly cemented samples (about 100 % cement content), where the brittle response leads to large local distortions of the correlation mesh and pronounced displacement jumps across cracks. In addition, the grain–cement skeleton in these specimens is comparatively stiff, undergoes only small deformations and appears more homogeneous with reduced grey-level contrast than weakly cemented material (e.g. about 20 % cement), which further reduces the robustness of the DVC results and increases their uncertainty at high cement contents. To mitigate these issues, an incremental DVC strategy was adopted: the initial configuration was correlated with the first loaded state, this first state

then served as the reference for the second load step, and so on. The incremental displacement fields were accumulated to obtain the displacement with respect to the initial state and yielded consistent results for weakly cemented specimens in the essentially linear-elastic regime. For strongly cemented samples, however, the apparent rigid-body contribution and the correlation error remained comparatively high, even with this stepwise strategy. Based on the displacement fields the shear strain and axial strain fields were derived for each phase and for the whole samples (goals 1,2,5).

Extension of the FEM-based numerical framework for fracture simulations (B5)

The extended finite element method (XFEM) implemented in ABAQUS/STANDARD was applied to the cemented specimens, and fracture and initiation energies were calibrated in a sensitivity study. For $S_{\text{cem}} = 100\,\%$ the final model (Fig. 8) shows an almost perfectly linear force–displacement response, indicating that XFEM cannot reproduce the experimentally observed brittle failure and post-peak softening. For CT-based cemented sands, the standard XFEM in ABAQUS is therefore only of limited suitability: although it represents displacement discontinuities without remeshing, it does not adequately capture the strongly heterogeneous microstructure. Consistent with Dong and Shin (2018) [L4] and the recommendations in the ABAQUS manual, the strong stiffness contrast between grains and cement combined with nonlinear damage and softening leads to numerical problems (poorly conditioned stiffness matrix, frequent cutbacks) and failure to reproduce the brittle post-peak response and the distributed microcracking visible in the CT images. Consequently, phase-field modeling (PFM) within the finite element framework was adopted. A UMAT model based on Navidteherani et al. (2021) [L5] was combined with coupled temperature–displacement elements by treating the phase-field variable as a pseudo-temperature. A new Python pre-processing code converts the CT-based geometry directly into an FE model with these elements, replacing the tetrahedral mesh tool from the first project phase. The implementation was extended by the star-convex split of Vicentini et al. (2024) [L6], enabling indirect control of the compressive-to-tensile strength ratio. Key parameters, including the critical energy release rate G_c, were identified in a sensitivity analysis. For $S_{\text{cem}} = 100\,\%$, the resulting force–displacement curve (Fig. 8) shows that the phase-field model reproduces the initial slope and peak load well, while the post-peak response remains more brittle than in the experiments. The results qualitatively show a shear-band-like propagation in the upper region, consistent with the experimentally observed failure behavior (Fig. 8) (goals 1–3).

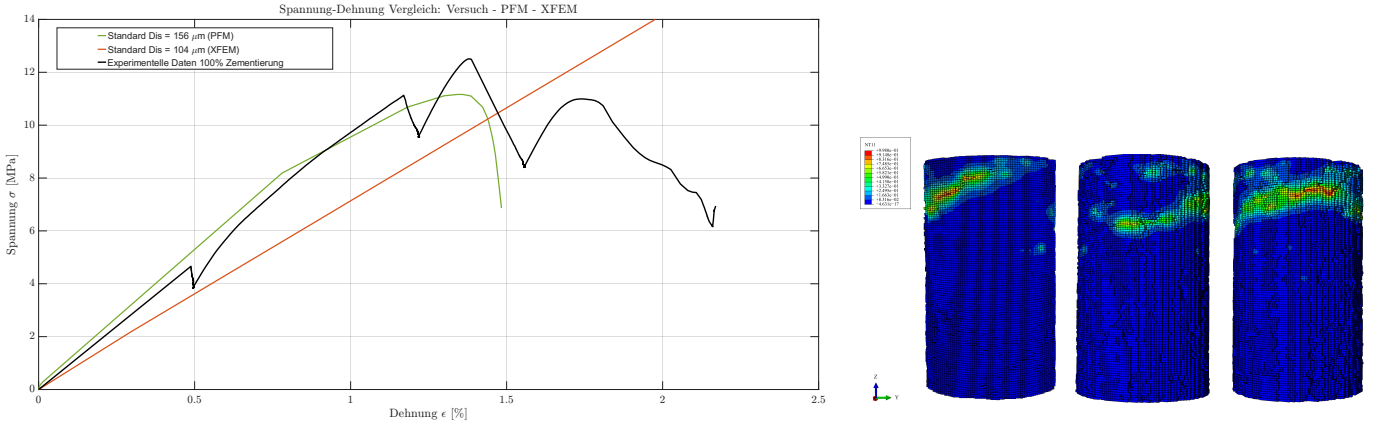

Figure 8: Validation of FEM results with experiments on stress–strain response (left), and crack pattern from FEM-PFM simulation (right) for $S_{\text{cem}} = 100\,\%$.

Extension of the FCM-based numerical framework for fracture simulations (M10)

Fracture occurs at higher loadings in the cemented sands. To efficiently predict crack initiation and propagation, PFM was incorporated into the FCM framework. The resulting FCM-PFM framework was further combined with non-negative moment fitting (NNMF) to reduce the integration effort, thereby accelerating the computations. This approach was validated on several 2D and 3D benchmarks, as well as a 3D example of a metal foam pore [A3, B1] (goal 3). Moreover, a hybrid implicit-explicit staggered scheme was developed to enhance robustness. This promising approach was also tested on a numerical example, demonstrating

significant potential for cemented sand simulations [B5] (goal 3). To model interfacial fracture, a novel fracture model was developed and incorporated into the FCM-PFM framework (goal 3). The idea is to reduce the fracture toughness at the material interfaces, where cracks are more likely to initiate. The resulting fracture toughness function exhibits a smooth transition between the interfaces, the cement matrix, and the grain particles. It is automatically constructed from the level-set function, obtained via L^2-projection. Although it exhibits kinks at the material interfaces, the resulting discontinuities in the integrands are already resolved by the previously mentioned integration schemes. Therefore, this approach is fully compatible with the developed extensions of the FCM. This method was tested on a 3D example of glass beads, using the same setup as in [A1]. Additional material and numerical fracture parameters were defined to complete the simulation setup. To neglect grain crushing, the fracture toughness of the grains was chosen to be much higher than that of the cement matrix. The results in Fig. 9 demonstrate that the proposed fracture modeling approach efficiently predicts interfacial fracture. Furthermore, large-scale simulations of the sample $S_{\text{cem}} = 100\,\%$ were performed on the supercomputers of NHR@ZIB, and the results were compared with experimental data, as shown in Fig. 10 (goal 2). Although the FCM-PFM shows good agreement with the experimental results up to the peak load, the load drops more rapidly in the post-peak region, indicating earlier fracture development. Here, the FCM-PFM yields a slope of $\overline{E}_{FCM-PFM} = 0.830\,\text{GPa}$ in the linear elastic regime, which is very close to the experimental value of $\overline{E}_{Exp} = 0.815\,\text{GPa}$ (with relative error of $\sim 2\,\%$). Moreover, the FCM-PFM predicts predominantly horizontal crack propagation, whereas the experimental results show vertically developing cracks. It is suggested that this behavior be investigated in future studies by considering alternative energy-splitting formulations. The findings are currently being prepared for a manuscript to be submitted to a journal.

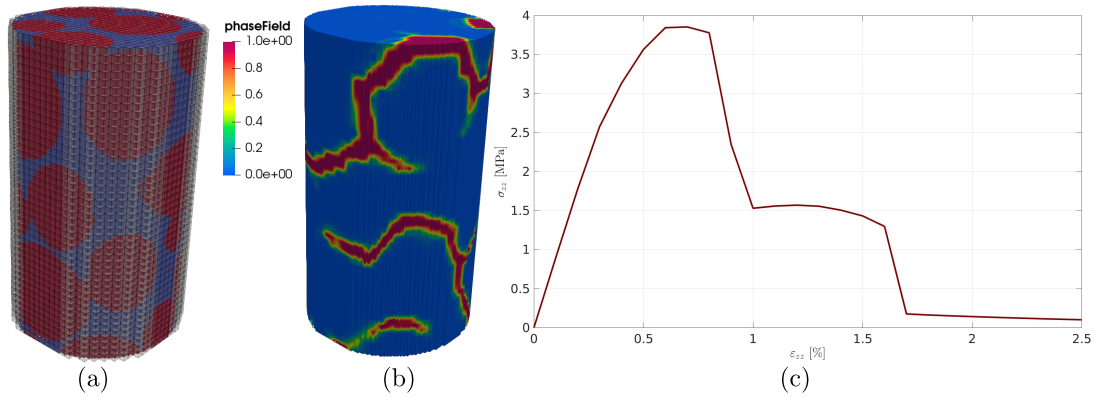

Figure 9: Fracture simulation of glass beads using FCM-PFM. (a) Geometry and mesh, (b) phase-field value at final load step, and (c) stress-strain curve.

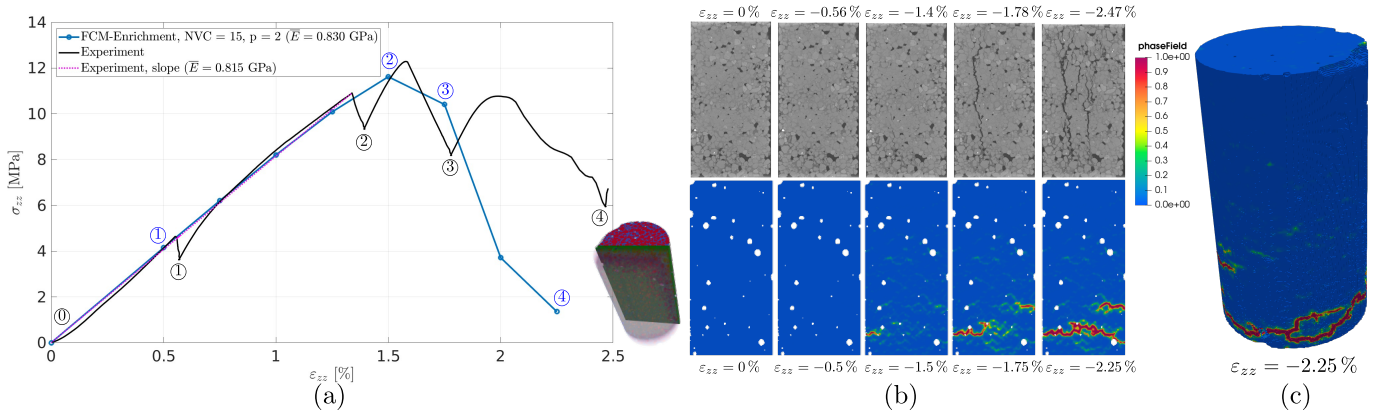

Figure 10: Fracture simulation of sample $S_{\text{cem}} = 100\,\%$ using FCM-PFM, and comparison with experiment. (a) Validation on stress-strain curve, (b) crack pattern at different loads (⓪ – ④), and (c) phase-field value at final load step.

Research Data

The macroscopic triaxial lab test data is available open-access and can be found in [U2]. The dataset contains the results of 175 triaxial compression tests on densely compacted cemented sand specimens with systematic variation of cementation degree and consolidation stress. The experimental data are provided

as CSV files including time series of axial displacement, load, volume change, and cell, radial and pore-water pressure. The CT scans from the second project phase (with cementation degrees of 20%, 30%, 40% and 80%) are available as open-access data via TORE [B3].

Miscellaneous

As part of his activities, Mahan Gorji, together with two TUHH colleagues, organized and ran the annual scientific *Continuum Mechanics Workshop 2022* with around 50 participants from TUHH and other universities, fostering scientific exchange and inter-university networking. To meet the high computational demands, the FCM code `AdhoC++` was ported to the high-performance computers at the Zuse Institute Berlin (NHR@ZIB, `https://nhr.zib.de/`), and extensive FEM simulations were carried out on the TUHH HPC cluster.

Literature

[L1] O. Stamati et al. `spam`: Software for Practical Analysis of Materials. *Journal of Open Source Software*, 5(51):2286, 2020.

[L2] J. N. Jomo. *Towards scalable finite cell computations on massively parallel systems*. Dissertation, Technische Universität München, 2021.

[L3] M. Gorji and A. Düster. Efficient simulation of heterogeneous materials with the finite cell method. In *Proceedings in Applied Mathematics & Mechanics*, volume 21, page e202100139, 2021.

[L4] X. Dong and Y. C. Shin. Crack formation within ceramics via coupled multiscale genome and XFEM predictions under various loading conditions. *Engineering Fracture Mechanics*, 204:517–530, 2018.

[L5] Y. Navidtehrani, C. Betegón, and E. Martínez-Pañeda. A simple and robust Abaqus implementation of the phase field fracture method. *Applications in Engineering Science*, 6:100050, 2021.

[L6] F. Vicentini, C. Zolesi, P. Carrara, C. Maurini, and L. De Lorenzis. On the energy decomposition in variational phase-field models for brittle fracture under multi-axial stress states. *International Journal of Fracture*, 247:291–317, 2024.

4 Published Project Results

4.1 Category A – Articles in peer-reviewed journals, contributions to peer-reviewed conferences or to anthology volumes, and book publications

[A1] M. Gorji, M. Komodromos, W. Garhuom, J. Grabe, and A. Düster. Geometry smoothing and local enrichment of the finite cell method with application to cemented granular materials. *Computational Mechanics*, 75:429–454, 2025, open access (OA).

[A2] S. F. Hosseini, M. Gorji, W. Garhuom, and A. Düster. Adaptive Quadrature of Trimmed Finite Elements and Cells Based on Bezier Approximation. *International Journal of Computational Methods*, 21:2350023, 2024.

[A3] S. F. Hosseini, M. Gorji, R. Sartorti, L. Radtke, and A. Düster. Application of the non-negative moment fitting approach in the finite cell analysis of brittle phase-field fracture. *International Journal for Computational Methods*, 22:2550022, 2025.

[A4] M. Komodromos, M. Gorji, A. Düster, and J. Grabe. Investigation of the load sustaining micro mechanisms of cemented sand using the mesoscale FEM approach. *Computers and Geotechnics*, 162:105656, 2023, OA.

[A5] M. Komodromos, M. Gorji, A. Düster, and J. Grabe. Implementation of linear strain elements for image-based Finite Element Analysis of cemented natural sand. *Computers and Geotechnics*, 174:106606, 2024.

4.2 Category B – Any other form of published results

[B1] M. Gorji, S. F. Hosseini, R. Sartorti, L. Radtke, and A. Düster. Acceleration of immersed computations of brittle phase-field fracture utilizing moment fitting schemes. *Proceedings in Applied Mathematics and Mechanics*, page e202400094, 2024, OA.

[B2] M. Gorji, M. Komodromos, J. Grabe, and A. Düster. Image-based analysis of complex microstructures using the finite cell method. *Proceedings in Applied Mathematics and Mechanics*, 22:e202200291, 2023, OA.

[B3] E. Hadjiloo, L. Sekulic, D. Dao, K. Cerek, and J. Grabe. Micro-CT Dataset of Cemented Sand Specimens under Uniaxial Compression with Varying Cementation Degree. TUHH TORE, 2026. OA, DOI: 10.15480/882.16483.

[B4] S. F. Hosseini, M. Gorji, and A. Düster. Accurate integration of trimmed cells based on Bezier approximation. *Proceedings in Applied Mathematics and Mechanics*, 22:e202200204, 2023, OA.

[B5] S. F. Hosseini, M. Gorji, R. Sartorti, L. Radtke, and A. Düster. Simulating brittle fracture with a robust hybrid explicit-implicit solver for staggered phase-field problems. *Proceedings in Applied Mathematics and Mechanics*, page e202400042, 2025, OA.

[B6] M. Komodromos, M. Gorji, A. Düster, and J. Grabe. Mesoscale FEM approach on cemented sand: challenges and implementation of high order elements. In L. Zdravkovic, S. Kontoe, D. M. G. Taborda, and A. Tsiampousi, editors, *Proceedings 10th NUMGE 2023*, 2023, OA.

[B7] M. Komodromos, M. Gorji, A. Düster, and J. Grabe. On the load bearing mechanisms of cemented granular material: A mesoscale FE approach. *Proceedings in Applied Mathematics and Mechanics*, 23:e202300037, 2023, OA.

[B8] L. Sekulic, E. Hadjiloo, K. Cerek, and J. Grabe. Experimental dataset of triaxial tests with cemented sand. TUHH TORE, 2025. OA, DOI: 10.15480/882.14959.

4.3 Patents (applied for and granted)